Differential reactivity of rutile and anatase TiO2 nanoparticles: synthesis and surface states of nanoparticles of mixed valence Magnéli oxides

Elham Baktash, Jérôme Capitolis, Lionel Tinat, Clément Larquet, Tsou Hsi Camille Chan Chang, Jean-Jacques Gallet, Fabrice Bournel, Clément Sanchez, Sophie Carenco, David Portehault

Differential reactivity of rutile and anatase TiO₂ nanoparticles: synthesis and surface states of nanoparticles of mixed valence Magnéli oxides

Elham Baktash,[a] Jérôme Capitolis,[a] Lionel Tinat,[a] Clément Larquet,[a] Tsou Hsi Camille Chan Chang,[a] Jean-Jacques Gallet,[b,c] Fabrice Bournel,[b,c] Clément Sanchez,[a] Sophie Carenco,[a] David Portehault*[a]

Abstract: Magnéli phases Ti_nO_{2n-1} (3 < n ≤ 10) are mixed Ti^{4+}/Ti^{3+} oxides with high electrical conductivity. When used for water remediation or electrochemical energy storage and conversion, they are nanostructured and exposed to various environments. Therefore, understanding their surface reactivity is of prime importance. Such studies have been hindered by carbon contamination from syntheses. Herein we address this synthetic and characterization challenge through a new approach towards 50 nm carbon-free Ti_4O_7 and Ti_6O_{11} nanoparticles. To do so, we take advantage of the different reactivities of rutile and anatase TiO_2 nanoparticles versus H_2, to use the former as precursors of Ti_nO_{2n-1} and the latter as diluting agents. This approach is combined to silica templating in order to restrain particles growth. The surface reactivity of the Magnéli nanoparticles under different atmospheres was then evaluated quantitatively with synchrotron radiation-based X-ray photoelectron spectroscopy, highlighting oxidized surfaces with lower conductivity than the core. This finding sheds a new light on the charge transfer occuring in these materials.
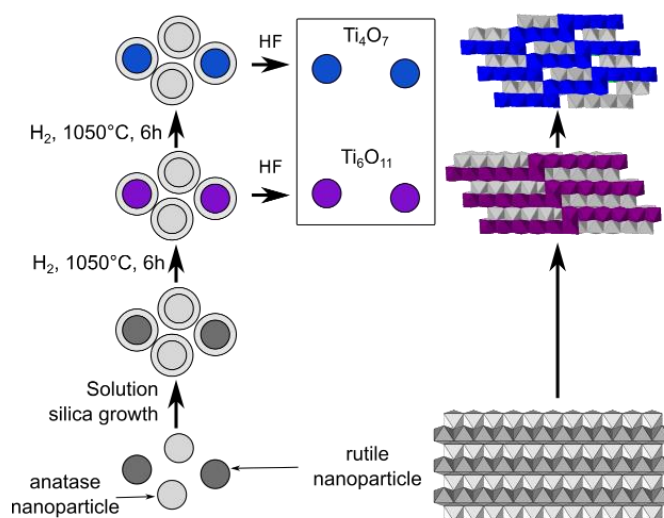
Figure 1. Scheme of the carbon-free process developed herein for the synthesis of freestanding nanoparticles of Magnéli phases. The approach combines silica templating, selective transformation of rutile TiO_2 into Magnéli phases, inability of the anatase polymorph to transform into Magnéli phases and selective solubilisation of silica and anatase into an aqueous solution of hydrofluoric acid.

Introduction

Titanium oxides Ti_nO_{2n-1} (4 ≤ *n* ≤ 10), so-called titanium Magnéli phases, were discovered in the 1950's[1] and experience since the 2010's a renewal of interest owing to their large conductivity and good stability, related to the mixed Ti^{4+}/Ti^{3+} valences and to their oxide nature, respectively. These properties have prompted the study of Magnéli phases in the late years as conductive scaffolds to be used in harsh conditions as cathodes for aprotic lithium-air[2–4] and lithium-sulfur batteries,[5–8] anodes for alcohols oxidation[9,10] and microbial fuel cells[11] as well as water remediation

membranes.[12,13] Superconductivity has also been recently evidenced in an epitaxially grown Magnéli phase.[14] Most of these studies not only take benefit from the conductivity of Magnéli phases, especially metallic Ti_4O_7, they also rely on their surface properties. For instance, many authors attribute the enhanced cyclability of Ti_4O_7-sulfur electrodes of Li-S batteries to the chemical bonding between sulfur atoms and Ti atoms at the surface of the Ti_4O_7 electrodes.[5–7] Likewise, Ti_4O_7 is considered as electrocatalyst[2] or electrocatalyst support[3,4] for air electrodes of Li-air batteries owing to their surface stability. For these reasons, increased surface-to-volume ratio is sought through nanostructuration, which emphases the importance of deep scrutinization of the composition and reactivity of Magnéli oxide surfaces. Although X-ray Photoelectron Spectroscopy (XPS) has shown that Ti^{4+} and Ti^{3+} coexist at the surface of Magnéli materials,[4,6,9,11,15] only two reports suggest surface oxidation of Ti_4O_7 materials,[2,8] but precise evaluation of surface states is lacking, so that the conduction and sorption properties of few nm-thick surface layers remain mostly a black box.

Nanostructured Magnéli phases can be produced by several approaches, including reduction of TiO_2 by Zr oxygen sponges[16] or plasmas.[17] However, most of the materials

[a]   Dr. E. Baktash, Dr. J Capitolis, L. Tinat, Dr. C. Larquet, Dr. T. H. C. Chan Chang, Prof. C. Sanchez, Dr. S. Carenco, Dr. D. Portehault
       Sorbonne Université, CNRS, Collège de France, Laboratoire de Chimie de la Matière Condensée de Paris (CMCP), 4 place Jussieu, F-75005, Paris, France
       E-mail: david.portehault@sorbonne-unversite.fr
[b]   Dr. J.-J. Gallet, Dr. F. Bournel
       Sorbonne Université, CNRS, Laboratoire de Chimie Physique, Matière et Rayonnement (LPCMR), 4 Place Jussieu, 75005 Paris, France
[c]   Dr. J.-J. Gallet, Dr. F. Bournel
       Synchrotron SOLEIL, L'Orme des Merisiers, Saint-Aubin, BP 48, 91192 Gif sur Yvette Cedex, France

       Supporting information for this article is given at the end of the document

reported above are produced by two main separate ways. The first pathway relies on carbothermal reduction of TiO_2 at ~800-1100 °C. It unavoidably produces carbon residues, accounting for 2 to ~20 wt. % of the samples.[5,7,8,18–21] These residues confine the oxide during the transformation of TiO_2 into Magnéli phases and enable recovering nanostructured materials. However, carbonaceous moieties are present at the surface of the Magnéli material. They can interfere in the oxide-electrolyte or oxide-sulfur/polysulfide interactions, thus making it difficult to draw conclusions about the respective role of the surfaces of the oxide and of the carbonaceous components. The second approach uses reduction of stoichiometric TiO_2 by dihydrogen at elevated temperature ~800-1100 °C.[3,4,6,11,13] In this route, crystal growth is difficult to restrain and leads to materials with submicronic length scale.[6,11,13] Attempts to limit grain growth by silica templating[3,4,15] encountered only limited success, leading mostly to 100-300 nm spheres[3,4] after dissolution of the silica coating.

Herein we propose an alternative method to produce carbon-free Magnéli nanoparticles (**Figure 1**) by reduction of a low cost commercial TiO_2 product, so-called P25, a mixture of nanoparticles of anatase and rutile TiO_2 polymorphs. In order to avoid extensive crystal growth during the crystallization of Magnéli phases, the approach takes benefit from silica templating and from the mechanism of formation of Magnéli phases, which occurs only in the rutile component through topotactic transformation. Therefore, anatase particles act only as diluting agents to further limit particle sintering. On the opposite, anatase particles can be selectively dissolved during a post treatment with hydrofluoric acid, in order to isolate the Magnéli nanoparticles. We then use these carbon-free nanoparticles as models to assess surface reactivity. Surface states are quantitatively probed by synchrotron radiation-based XPS for the pristine nanoparticles and after exposure to different atmospheres.

Results and Discussion

1. Synthesis and characterization of carbon-free Magnéli nanoparticles

Commercially available P25 titania was used as titanium precursor. This powder contains a mixture of anatase and rutile TiO_2 (80 wt. % anatase and 20 wt. % rutile) with ~35 nm particle size as shown by transmission electron microscopy (TEM) (**Figure 2**a). Silica-coated TiO_2 nanoparticles were prepared via the Stöber method[22] from tetraethyl orthosilicate as silica precursor added to an alcoholic suspension of P25 in basic conditions. TEM (**Figure 2**b) confirms that TiO_2-SiO_2 core-shell nanoparticles are obtained, with an 8 nm-thick silica shell showing lower contrast than the crystalline TiO_2 core. A similar SiO_2 shell is observed when grown on pure rutile particles (**Figure S1**). These particles were dried and the powders were heated at 1050 °C under reducing atmosphere (H_2/Ar, 5/95 vol. %) for 3, 6, 9 and 12 h. TEM (**Figure 2**c-e) shows that nanoparticles are obtained at 6 h and 12 h, still with surrounding silica, also observed from rutile nanoparticles (**Figure S1**). HRTEM (**Figure 2**d, f) indicates that the particles are made of Ti_6O_{11} and Ti_4O_7 at 6 and 12 h, respectively. This is confirmed by powder X-

Ray Diffraction (XRD, **Figure 3**) that also indicates minor amounts of crystalline anatase TiO_2 with Ti_4O_7. As expected, increasing the reduction time yields further reduction, from the semiconductor Ti_6O_{11} Magnéli phase to metallic Ti_4O_7 (**Figures** 2 and **3**). The stability of anatase, not the most stable polymorph in the bulk phase, suggests that some anatase nanoparticles are sufficiently stable to stand harsh thermal conditions. Indeed, anatase becomes the most stable polymorph of TiO_2 for nanoparticles smaller than ~10 nm.[23] Then, in the size range of P25 particles, the relative stabilities of anatase and rutile are close and yield coexistence of both polymorphs. As anatase particles growth is restricted by the silica coating, the smallest TiO_2 particles are stable in the anatase polymorph and do not convert into TiO_2 rutile. Rutile is a crucial intermediate for the formation of Magnéli phases through topotactic transformation by formation of shear planes (**Figure 1**),[18,19,24] so that hindering its formation also hinders the formation of Magnéli phases. Both silica and anatase dissolve in an hydrofluoric acid solution, while rutile TiO_2 phase does not react.[25] Because of the structural similarity between rutile and Magnéli phases, one can expect similar inertness versus hydrofluoric acid. Therefore, the samples were treated with an aqueous HF solution of diluted hydrofluorhydric acid (5 % vol.) to remove anatase and silica by-products. After washing, anatase remained only as minor impurity, while the Magnéli crystal structures were preserved (**Figure 3**). No particle
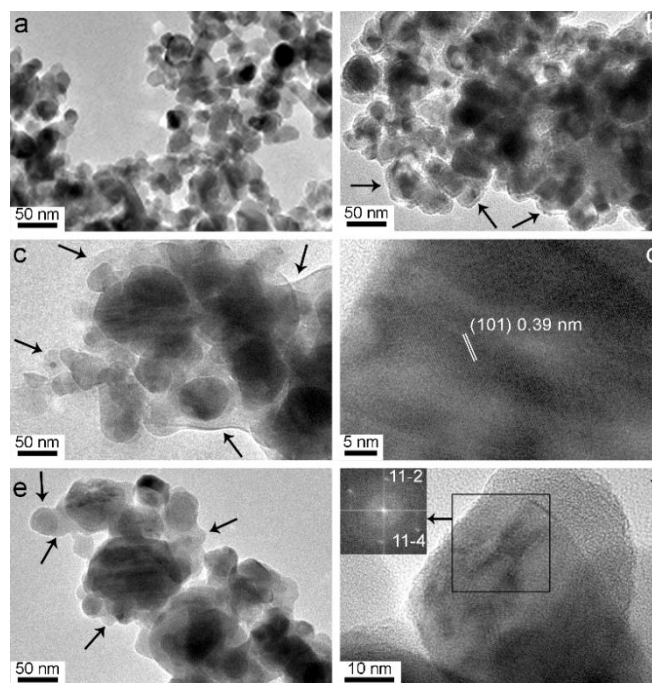

Figure 2. TEM images of (a) TiO_2 P25 nanoparticles, (b) TiO_2-SiO_2 core-shell particles. TEM (c) and HRTEM (d) of Ti_6O_{11} particles embedded into silica after thermal treatment (6 h). TEM (e) and HRTEM (f) of Ti_4O_7 particles embedded into silica after thermal treatment (12 h). Black arrows highlight silica, also shown in zooms-in Figure S1.
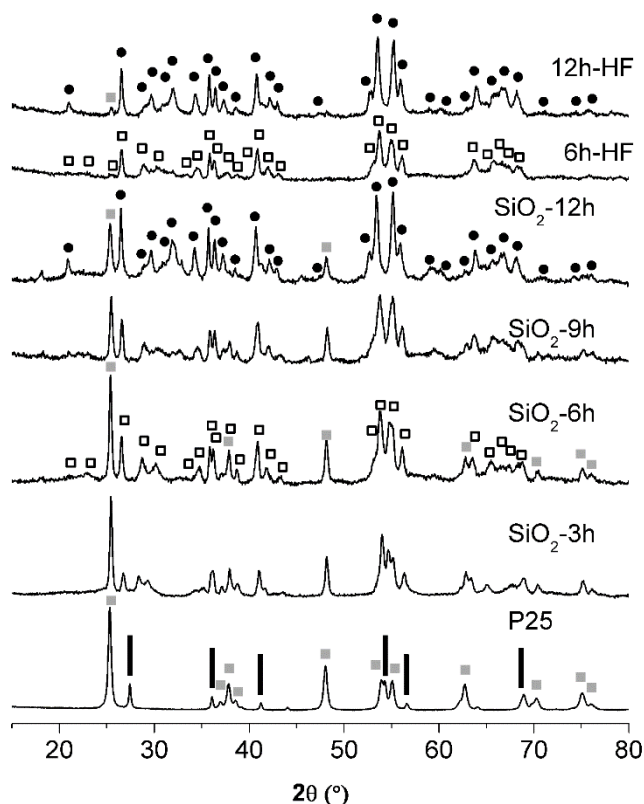
Figure 3. Powder XRD patterns of P25 titanium oxide particles in their pristine state and embedded into silica after heat treatment under H_2 (5 vol. % in argon) during 3 h, 6 h, 9 h and 12 h. The samples obtained at 6 h and 12 h have been treated in hydrofluoric acid 5 vol. % in order to recover Ti_6O_{11} and Ti_4O_7 nanoparticles, respectively. The peaks are indexed according to anatase TiO_2 (■), rutile TiO_2 (▌), Ti_6O_{11} (□), Ti_4O_7 (●).
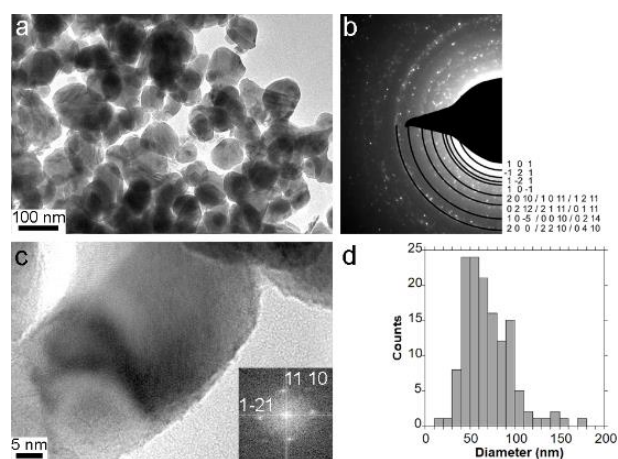
Figure 4. (a) TEM image, (b) SAED pattern, (c) HRTEM image and (d) size distribution of Ti_6O_{11} nanoparticles obtained after hydrofluoric acid treatment. The SAED pattern and HRTEM image are indexed along the Ti_6O_{11} structure.
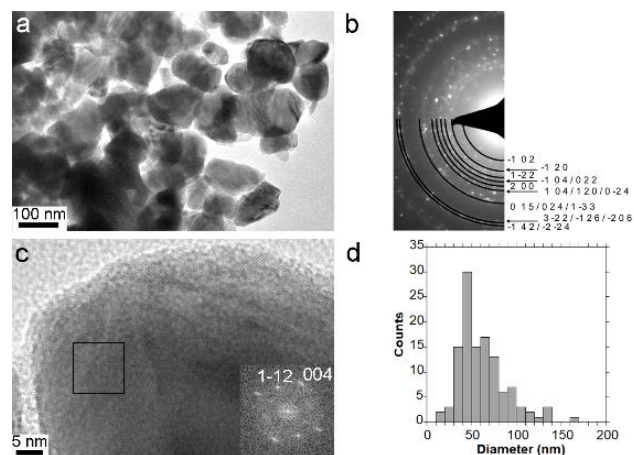

Figure 5. (a) TEM image, (b) SAED pattern, (c) HRTEM image and (d) size distribution of Ti_4O_7 nanoparticles obtained after hydrofluoric acid treatment. The SAED pattern and HRTEM image are indexed along the Ti_4O_7 structure.

smaller than 10 nm could be distinguished by TEM (**Figures 4** and **5**) and silicon was not anymore detected by XPS. HRTEM images and Selected Area Electron Diffraction (SAED) patterns are fully indexed along the Ti_6O_{11} (**Figure 4**) and Ti_4O_7 (**Figure 5**) structures, respectively. The size distributions (**Figures 4** and **5**) for both Ti_6O_{11} and Ti_4O_7 samples indicate that the nanoparticle size increased after treatment at high temperature, with distribution maxima for diameters of *ca.* ~50 nm. The occurrence of minor amounts of particles larger than 80 nm suggests that at 1050 °C, the silica coating experiences local rearrangements and does not act as a perfect barrier against particle growth. However, severe particle growth of the titanium oxide particles is clearly limited thanks to the combined action of silica and anatase particles against sintering. Indeed, a reference sample produced by heat treatment for 12 h of pure rutile nanoparticles embedded in silica yield particles larger than 100 nm in average (**Figure S1**). Hence, non- reactive anatase nanoparticles are crucial for hindering Magnéli particles sintering through a dilution effect. Overall, the Magnéli oxides Ti_6O_{11} and Ti_4O_7 can be obtained as crystalline nanoparticles of 50 nm, respectively.

In order to assess the surface reactivity of the silica-free Magnéli nanoparticles versus different atmospheres, we have probed the average oxidation state of titanium near the surface by X-ray Photoelectron Spectroscopy (XPS) induced by synchrotron radiation. Adjusting the incident energy enabled tuning the probed depth and then retrieving depth profiles of Ti oxidation state.[26]

2. Surface state of as-obtained Magnéli nanoparticles

The Ti_6O_{11} and Ti_4O_7 nanoparticles were analysed after synthesis and purification with hydrofluoric acid in their initial state (**Figures 4** and **5**). The survey XPS spectra are provided as **Figure S2**. The photon energies were fixed at 560, 735 and 950 eV, corresponding for Ti2p to electron kinetic energies of 100, 390 and 490 eV, then to depths of analysis (Inelastic Mean Free Path IMFP) of 0.6, 0.9 and 1.3 nm, hence 2, 3 and 4 TiO_6 octahedra, respectively.[27] Spectra of the Ti 2p region of the fresh
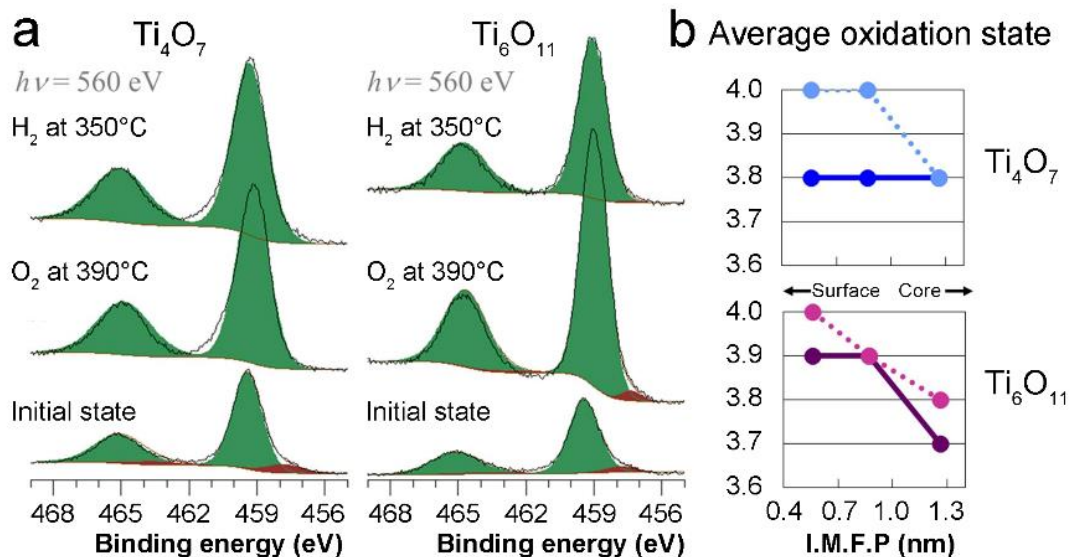
Figure 6. (a) Ti 2p X-ray photoelectron spectra of Ti_4O_7 and Ti_6O_{11} nanoparticles collected with a photon energy of 560 eV (IMFP 0.6 nm corresponding to the first top TiO_6 octahedra layer). Ti(IV) species are in green and Ti(III) species in brown. Spectra were recorded at the initial state, after exposure to O_2 (0.2 mbar) at 390 °C and then after exposure to H_2 (1.0 bar at 350 °C). Average oxidation states (b) of both samples are plotted for the initial state (plain lines) and the oxidized state (dotted lines) as a function of the IMFP (depth analysis).
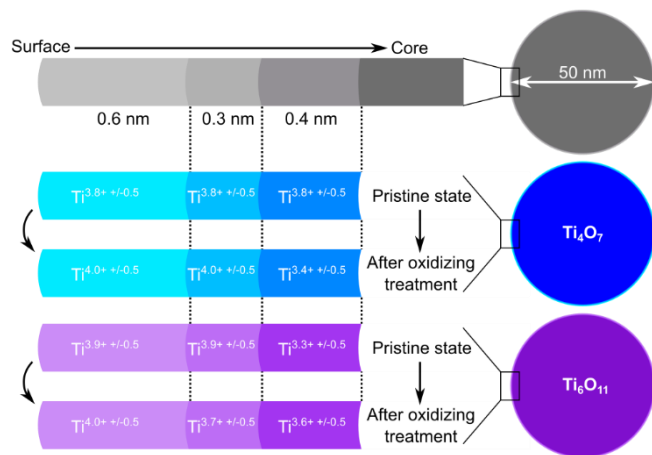
Figure 7. Depth profiles of the average oxidation state of titanium for Ti_4O_7 and Ti_6O_{11} nanoparticles in their initial state (a) and after oxidation under 0.2 mbar of O_2 at 390 °C (b). The oxidation states are evaluated from the Ti 2p X-ray photoelectron spectra at different incident energies, eg. different IMFP values, hence different probed thicknesses. The three layers from the surface to the core correspond to the first and second (0.6 nm), third (0. 3 nm) and fourth (0.4 nm) TiO_6 octahedra layers, respectively.

nanoparticles (**Figures 6**a and **S3** for IMFP 0.6 nm, **Figures S4** and **S5** for all IMFPs) show two unambiguous contributions: one for Ti(IV) species (green) and one for Ti(III) species (brown), each of them a doublet with a splitting of about 5.7 eV. The two contributions are separated by 1.6 eV, in agreement with previous

reports.[28,29] The fitting procedure (details in the experimental section and SI) allows calculating the average Ti oxidation state through each probed depth (**Figure 6**b). Due to the fairly low amount of Ti(III) near the surface, the precision on the average oxidation state is ± 0.1. The expected oxidation states of Ti_4O_7 and Ti_6O_{11} are respectively 3.50 and 3.67. We observe higher oxidation state than expected: 3.8 for Ti_4O_7 and a gradient from 3.9 to 3.7 for Ti_6O_{11}, from the very surface to a depth of ~1.3 nm for Ti_6O_{11}. These results are confirmed by the O 1s region of the XPS spectra (**Figure S6**). This behaviour is in agreement with two previous works qualitatively showing surface oxidation of Magnéli materials produced by carbothermal reduction, hence containing carbon residues.[2,8] Here we not only show that surface oxidation occurs even with carbon-free Magnéli phases, but we also quantify the average Ti oxidation state. Although the XPS measurements are performed on a powder deposited on a substrate,[26] one can propose a simple model of the depth profile of the Ti oxidation state, based a simple 3-layers model from the three depths probed by XPS (**Figure 7**).[26] Note that the Ti oxidation state most probably evolves through a gradient from the surface to core, so that the layered model shown here is a simplification. Ti^{3+} is present at the surface of Ti_4O_7 and Ti_6O_{11}, ensuring charge transfer during interfacial events occurring in thermoelectric energy conversion,[18] electrochemical water remediation[12,13] or charge storage.[2–8] However, the low Ti^{3+} amount in the first three octahedra layers corresponds to a composition closer to $Ti_{10}O_{19}$ than Ti_4O_7 or Ti_6O_{11}, hence a semiconducting layer instead of a metallic phase as expected from Ti_4O_7. This result suggests that accurate evaluation of sorption properties must take into account such surface oxidation.[6] Given XPS measurement uncertainties (**Figure 7**),

the buried layer corresponding to the fourth TiO_6 octahedra layer reaches compositions close to the nominal compounds Ti_4O_7 and Ti_6O_{11}, respectively. A gradual decrease of the average oxidation state deeper into the particle core is likely to occur and yield the Ti_4O_7 and Ti_6O_{11} detected by XRD.

3. Surface reactivity of Magnéli nanoparticles

In order to assess the surface reactivity of the Magnéli phases, we exposed the nanoparticles to oxidizing conditions. O_2 (0.2 mbar) was introduced in the chamber and the samples were heated up to 390 °C. Spectra were collected after cooling the samples and pumping the gas atmosphere (**Figure 6**a for IMFP 0.6 nm and **Figures S7** and **S8** for all IMFPs). The average oxidation state has been evaluated from the fit of these curves (dotted lines on **Figure 6**b). For the first two Ti atom layers (IMFP = 0.6 nm), complete conversion of Ti(III) to Ti(IV) was observed for both Ti_4O_7 and Ti_6O_{11}. Deeper below the surface (**Figures 6**b and **7**), more reduced states were observed. Therefore, close to the core, some Ti(III) species survived the oxidizing treatment and the surface layer of TiO_2 acted as a passivation layer. Note that at similar temperatures but higher pressure of oxygen (1 bar), thermogravimetric analysis shows that Ti_4O_7 experiences complete oxidation into TiO_2.[18]

We attempted to reduce back the surface Ti(IV) species into Ti(III) by exposing the nanoparticles to 1 bar of H_2 under heating up to 350 °C for 10 minutes. The samples were again analyzed after cooling and outgasing (**Figure 6**a for IMFP 0.6 nm, other IMFPs not shown). No significant change in the oxidation states was observed, indicating that in such conditions, surface oxidation is not reversible and reduction would need higher temperatures.

4. Conduction properties

Because XPS depends strongly on the ability of the material to extract the charges produced by incident X-ray radiation, the technique is suitable to sort qualitatively different materials in terms of electric conductivity and electronic structure. Each Ti 2p spectrum was calibrated over Au 4f spectrum, collected within minutes. Within the spectral resolution of the beamline (<0.1 eV), charging effects were observed in the Ti 2p region. At each step of the thermal treatment, the Ti $2p_{3/2}$ binding energy (B.E.) of the Ti(IV) species was used as an indicator of this charging effect (**Figure 8**).

For each incident energy, B.E. for Ti_4O_7 shows a negligible variation, between 0 and 0.2±0.1 eV (**Figure 8**a). For Ti_6O_{11} (**Figure 8**b) these variations are between 0.1 and 0.4 eV, the main effect being observed from the initial state to the oxidized state, where the variation is between 0.3 and 0.4 eV, which represents significant surface charging. Charging effects observed here are thus compatible with the higher conductivity reported for Ti_4O_7 than for Ti_6O_{11}, in the bulk state.[30] More important, this study also shows that even if Ti_4O_7 is oxidized at the surface under oxygen at 390 °C, it is still more conductive (higher B.E.) than oxidized Ti_6O_{11}, and a *fortiori* TiO_2. Thus, if surface oxidation impacts the first three TiO_6 octahedra layers at the surface of the particles, Magnéli phases and especially Ti_4O_7 maintain high conductivity. Note also that after treatment under H_2, the conductivity is increased (**Figure 8**), although no significant change in the

surface oxidation state of Ti is observed. This evolution could arise from the formation of small amounts of Ti^{3+} within the uncertainty range of the XPS measurements. The conductivity enhancement could also be related to the creation of a disordered surface layer, well documented for black anatase produced by reacting H_2 with stoichiometric TiO_2 in the same temperature range.[31,32]
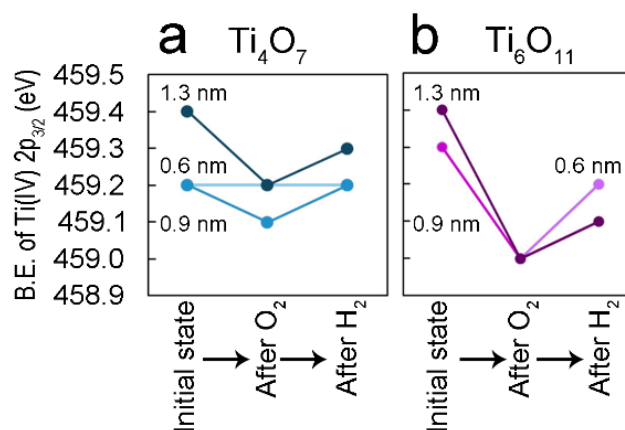
Figure 8. Binding energies (B.E.) of Ti(IV) $2p_{3/2}$ species for (a) Ti_4O_7 and (b) Ti_6O_{11}. The darker, intermediate and lighter lines stand for the data collected at 950, 735 and 560 eV, respectively. The corresponding IMFPs are given. The measurement error of B.E. is 0.1 eV.

Conclusions

In this work we have reported two advances. We have first described a simple approach to produce carbon-free nanoparticles of Magnéli phases with diameter approx. 50 nm and controlled stoichiometry. This achievement was made possible by combining silica templating and the large difference in reactivity of two different TiO_2 polymorphs: while rutile TiO_2 nanoparticles transform into Magnéli phases upon reduction, anatase TiO_2 nanoparticles do not yield Magnéli phases and can act as diluting agents to avoid severe sintering of the Magnéli nanoparticles. On the opposite, anatase is more reactive towards hydrofluoric acid than Magnéli phases, so that it can be selectively dissolved together with the silica template and produce freestanding Magnéli nanoparticles. Such nanoparticles without surface carbonaceous moieties appear as excellent models to assess quantitatively the surface reactivity of Magnéli nanostructures. Sensitivity to oxidation under ambient conditions has been evidenced for the first surface layers of TiO_6 octahedra. Note that this surface oxidation could also be partly related to short exposure to aqueous diluted hydrofluoric acid in order to dissolve silica and anatase components. This question should be addressed in the future. These results should enlighten the properties of interfaces between Magnéli materials and various electrolytes or electrode materials, such as sulphur or lithium oxides,[2,5,6] in order to design advanced energy storage and remediation devices.

Experimental Section

Materials. P25 titania, tetraethyl orthosilicate (TEOS) (99.999%), ammonia aqueous solution (28-30%) and ethanol (99.5%) were purchased from Sigma–Aldrich. Pure rutile nanoparticles were purchased from SSNano. All chemicals were reagent grade and used without further purification.

Synthesis. 1.0 g of P25 and 1.34 mL of ammonia solution were added into 10 mL ethanol. The mixture was dispersed using ultrasonication for about 30 min. 1.9 mL of TEOS was added dropwise to the dispersion during 45 min. The concentration of TEOS after addition into the dispersion was 0.85 M. The reagents molar ratio correspond to Si/Ti = 0.68. After stirring overnight, the reaction mixture was centrifuged at 15000 rpm for 10 min. The supernatant was removed, the resulting core-shell TiO_2-SiO_2 nanoparticles were washed with ethanol by three cycles of centrifugation-redispersion and then dried overnight at room temperature under vacuum. In the next step, TiO_2-SiO_2 nanoparticles were heated to 1050 °C at 10 °C·min^{-1} under reducing atmosphere (H_2/Ar, 5:95 vol.) for different periods to yield silica-coated Magnéli particles. Finally some selected samples were treated with an HF solution 5 vol. % for 15 min. They were then washed three times with MilliQ water and dried under vacuum at room temperature overnight.

Powder X-Ray Diffraction (XRD) was performed on a D8 Bruker diffractometer operating at Cu-Kα radiation in the Bragg-Brentano configuration. The XRD patterns were indexed along the ICSD cards 9852, 9161, 35121 and 16297 for anatase TiO_2, rutile TiO_2, Ti_6O_{11}, Ti_4O_7.

Transmission Electron Microscopy (TEM) was performed on a Tecnai Spirit microscope operating at 120 kV. Samples were prepared by drop-casting of a suspension of nanoparticles on a carbon-coated copper grid. SAED patterns were calibrated according to the pattern of a sample made of gold nanoparticles. The patterns were indexed along the crystallographic references listed above in the XRD section.

X-ray photoelectron spectroscopy (XPS). XPS experiments were performed on the NAP-XPS end-station of Sorbonne Université set on the TEMPO beamline at SOLEIL synchrotron (Saint-Aubin, France). The hemispheric electron analyzer is a Phoibos 150 NAP apparatus (SPECS). The samples were prepared by dip-coating. Nanoparticles suspended in ethanol were deposited on a silicon wafer coated with a 50 nm thick gold layer. The XPS spectra were calibrated according to the Au $4f_{7/2}$ signal at 84.0 eV. Using CasaXPS software package, the Ti 2p regions were fitted with two doublets Ti $2p_{3/2}$/Ti $2p_{1/2}$ corresponding to Ti(III) and Ti(IV) (see supporting information). For both contributions the background was fitted by a Shirley background and the components by a Gaussian/Lorentzian product GL(30) line shape. Details of the fitting constraints are given in supporting information. The average oxidation state for Ti in the probed layer was then evaluated according to the following formula:

$$\Delta ox_{mean} = 3 * \left(\frac{A\,Ti(III)}{A\,Ti(III) + A\,Ti(IV)} \right) + 4 * \left(\frac{A\,Ti(IV)}{A\,Ti(III) + A\,Ti(IV)} \right)$$

In this formula, Δox_{mean} is the average oxidation state for Ti in the probed layer. ATi(III) and ATi(IV) are the area of the 2p $_{3/2}$ peak of titanium at oxidation state III and IV, respectively.

Acknowledgements

[1]   S. Andersson, B. Collén, U. Kuylenstierna, A. Magnéli, *Acta Chem. Scand.* **1957**, *11*, 1641.

[2]   D. Kundu, R. Black, E. J. Berg, L. F. Nazar, *Energy Environ. Sci.* **2015**, *8*, 1292.

[3]   X. Cao, Z. Sun, X. Zheng, J. Tian, C. Jin, R. Yang, F. Li, P. He, H. Zhou, *J. Mater. Chem. A* **2017**, *5*, 19991.

[4]   S. Lee, G. H. Lee, J. C. Kim, D. W. Kim, *ACS Catal.* **2018**, *8*, 2601.

[5]   Q. Pang, D. Kundu, M. Cuisinier, L. F. Nazar, *Nat. Commun.* **2014**, *5*, 4759.

[6]   X. Tao, J. Wang, Z. Ying, Q. Cai, G. Zheng, Y. Gan, H. Huang, Y. Xia, C. Liang, W. Zhang, Y. Cui, *Nano Lett.* **2014**, *14*, 5288.

[7]   S. Mei, C. J. Jafta, I. Lauermann, Q. Ran, M. Kärgell, M. Ballauff, Y. Lu, *Adv. Funct. Mater.* **2017**, *27*, 1.

[8]   H. Wei, E. F. Rodriguez, A. S. Best, A. F. Hollenkamp, D. Chen, R. A. Caruso, *Adv. Energy Mater.* **2017**, *7*, DOI 10.1002/aenm.201601616.

[9]   C. He, S. Chang, X. Huang, Q. Wang, A. Mei, P. K. Shen, *Nanoscale* **2015**, *7*, 2856.

[10]   P. K. Shen, C. He, S. Chang, X. Huang, Z. Tian, *J. Mater. Chem. A* **2015**, *3*, 14416.

[11]   M. Ma, S. You, G. Liu, J. Qu, N. Ren, *J. Mater. Chem. A* **2016**, *4*, 18002.

[12]   P. Geng, J. Su, C. Miles, C. Comninellis, G. Chen, *Electrochim. Acta* **2015**, *153*, 316.

[13]   P. Geng, G. Chen, *J. Memb. Sci.* **2016**, *498*, 302.

[14]   K. Yoshimatsu, O. Sakata, A. Ohtomo, *Sci. Rep.* **2017**, *7*, 1.

[15]   C. Yao, F. Li, X. Li, D. Xia, *J. Mater. Chem.* **2012**, *22*, 16560.

[16]   A. Kitada, G. Hasegawa, Y. Kobayashi, K. Kanamori, K. Nakanishi, H. Kageyama, *J. Am. Chem. Soc.* **2012**, *134*, 10897.

[17]   A. F. Arif, R. Balgis, T. Ogi, F. Iskandar, A. Kinoshita, K. Nakamura, K. Okuyama, *Sci. Rep.* **2017**, *7*, 3646.

[18]   D. Portehault, V. Maneeratana, C. Candolfi, N. Oeschler, I. Veremchuk, Y. Grin, C. Sanchez, M. Antonietti, *ACS Nano* **2011**, *5*, 9052.

[19]   V. Maneeratana, D. Portehault, J. Chaste, D. Mailly, M. Antonietti, C. Sanchez, *Adv. Mater.* **2014**, *26*, 2654.

[20]   S. Qian, J. Mao, *J. Mater. Sci. Mater. Electron.* **2015**, *26*, 5166.

[21]   S. S. Huang, Y. H. Lin, W. Chuang, P. S. Shao, C. H. Chuang, J. F. Lee, M. L. Lu, Y. T. Weng, N. L. Wu, *ACS Sustain. Chem. Eng.* **2018**, *6*, 3162.

[22]   X. Feng, S. Zhang, X. Lou, *Colloids Surf. B Biointerfaces* **2013**, *107*, 220.

[23]   A. S. Barnard, *Reports Prog. Phys.* **2010**, *73*, 86502.

[24]   S. Tominaka, Y. Tsujimoto, Y. Matsushita, K. Yamaura, *Angew. Chem. Int. Ed. Engl.* **2011**, *3*, 2.

[25]   T. Ohno, K. Sarukawa, K. Matsumura, *J. Phys. Chem.* **2001**, *105*, 2417.

[26]   D. D. Sarma, P. K. Santra, S. Mukherjee, A. Nag, *Chem. Mater.* **2013**, *25*, 1222.

[27] S. Tanuma, C. J. Powell, D. R. Penn, *Surf. Interface Anal.* **1994**, *21*, 165.

[28] J. Pouilleau, D. Devilliers, H. Groult, P. Marcus, *J. Mater. Sci.* **1997**, *32*, 5645.

[29] M. C. Biesinger, L. W. M. Lau, A. R. Gerson, R. S. C. Smart, *Appl. Surf. Sci.* **2010**, *257*, 887.

[30] F. C. Walsh, R. G. A. Wills, *Electrochim. Acta* **2010**, *55*, 6342.

[31] M. Tian, M. Mahjouri-Samani, G. Eres, R. Sachan, M. Yoon, M. F. Chisholm, K. Wang, A. A. Puretzky, C. M. Rouleau, D. B. Geohegan, G. Duscher, *ACS Nano* **2015**, *9*, 10482.

[32] K. Zhang, J. H. Park, *J. Phys. Chem. Lett.* **2017**, *8*, 199.
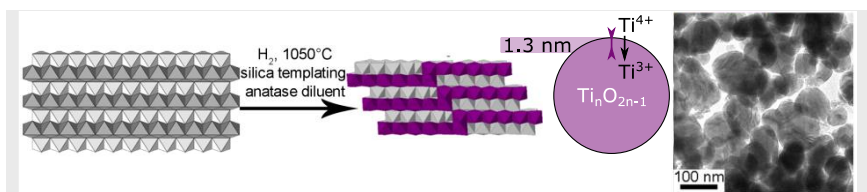
A new route to nanoparticles of Ti_nO_{2n-1} mixed valence oxides with controlled size distribution is described, by combining a templating strategy with the different reactivities of two TiO_2 polymorphs. Synchrotron radiation-based photoelectron spectroscopy reveals for the first time the surface reactivity of these carbon-free nanoparticles.

Elham Baktash, Jérôme Capitolis, Lionel Tinat, Clément Larquet, Tsou Hsi Camille Chan Chang, Jean-Jacques Gallet, Fabrice Bournel, Clément Sanchez, Sophie Carenco, David Portehault*

Differential reactivity of rutile and anatase TiO₂ nanoparticles: synthesis and surface states of nanoparticles of mixed valence Magnéli oxides

The constraints used to fit Ti 2p X-ray photoelectron spectra are the following:[29]

|	Ti(IV) 2p 3/2	Ti(IV) 2p 1/2	Ti(III) 2p 1/2	Ti(III) 2p 3/2
Area (a.u.)	-	(Ti(IV) 2p3/2)*0.5	-	(Ti(III) 2p1/2)*0.5
FWHM (eV)	1-2	1-3	1-3	1-3
Binding energy (eV)	B-5.77	471-450	B-7.17	B-1 .57

A typical result of the fitting procedure is detailed below, on the example of Ti_4O_7 in the pristine state:

|	Ti(IV) 2p 3/2	Ti(IV) 2p 1/2	Ti(III) 2p 1/2	Ti(III) 2p 3/2
Area (a.u.)	209035	104518	33992	16996
FWHM (eV)	1.47	2.37	2.58	3.00
Binding energy (eV)	459.25	465.02	457.85	463.45
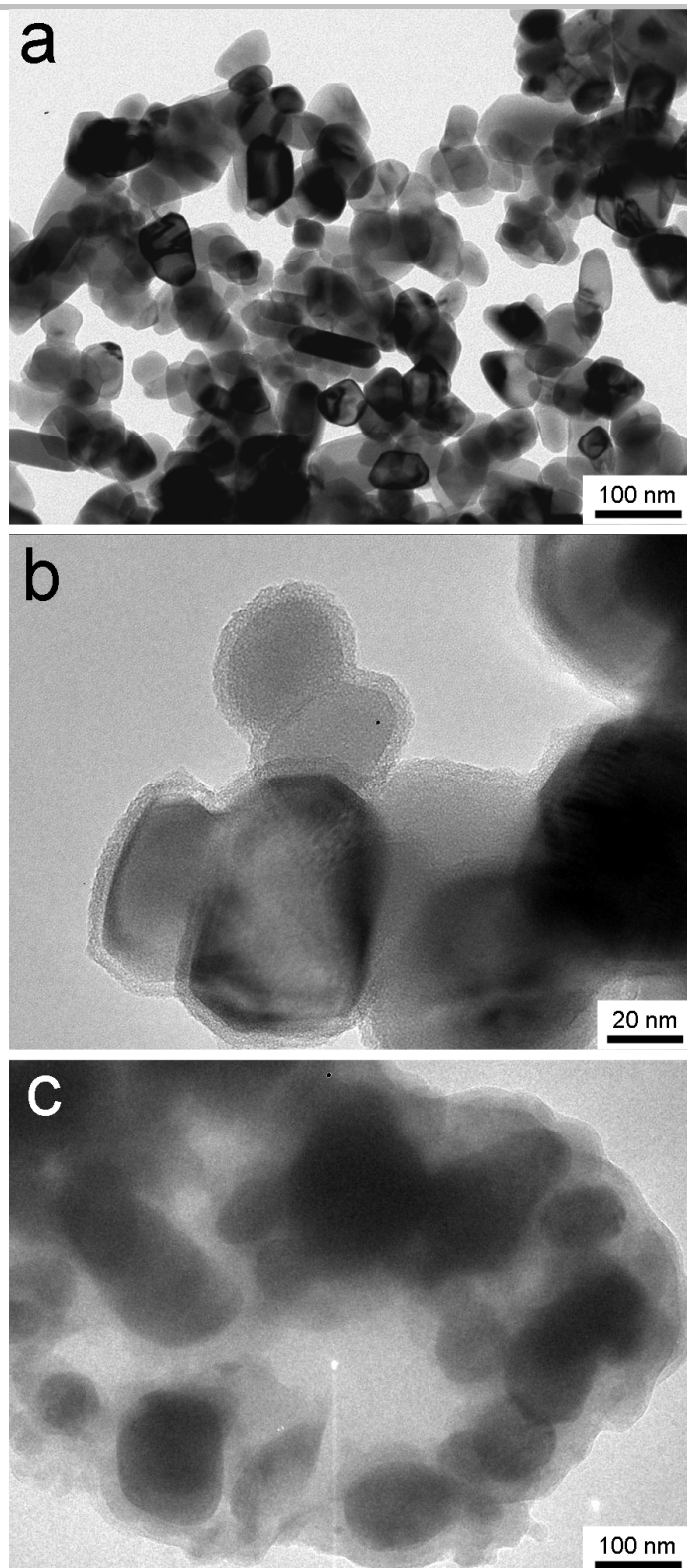
Figure S1. TEM images of (a) pure rutile particles, (b) the same rutile particles embedded in silica shells, (c) Ti_4O_7 particles obtained by reductive treatment at 12 h of the rutile particles embedded in silica. Large particle growth can be observed.
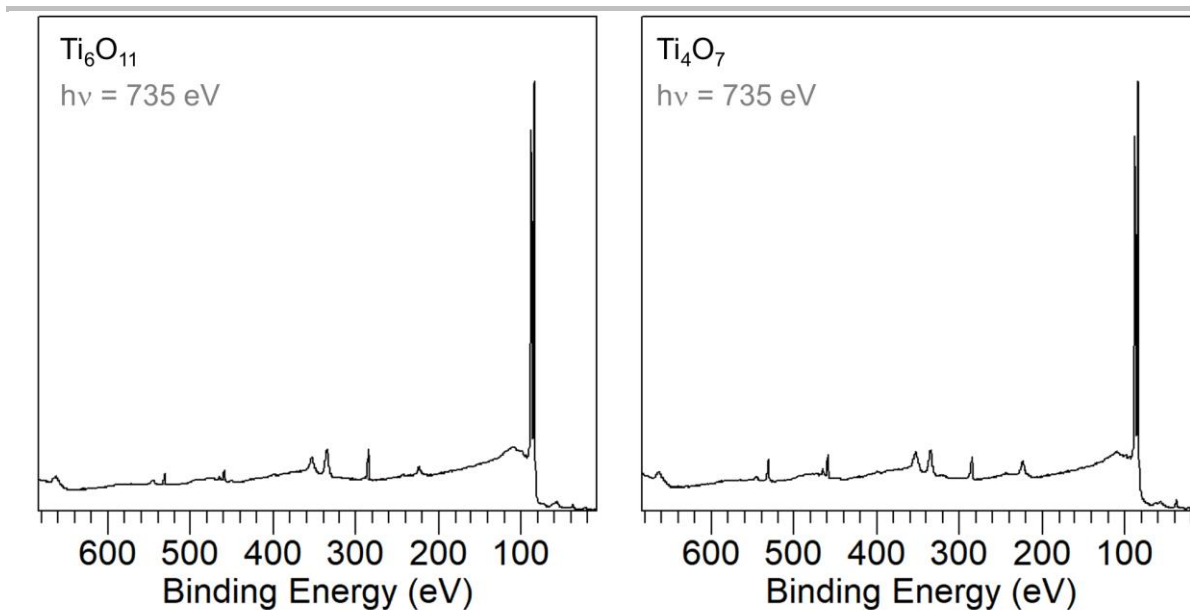
**Figure S2.** Survey XPS spectra of Ti_6O_{11} and Ti_4O_7 nanoparticles at their initial state, after removal of the silica shell.
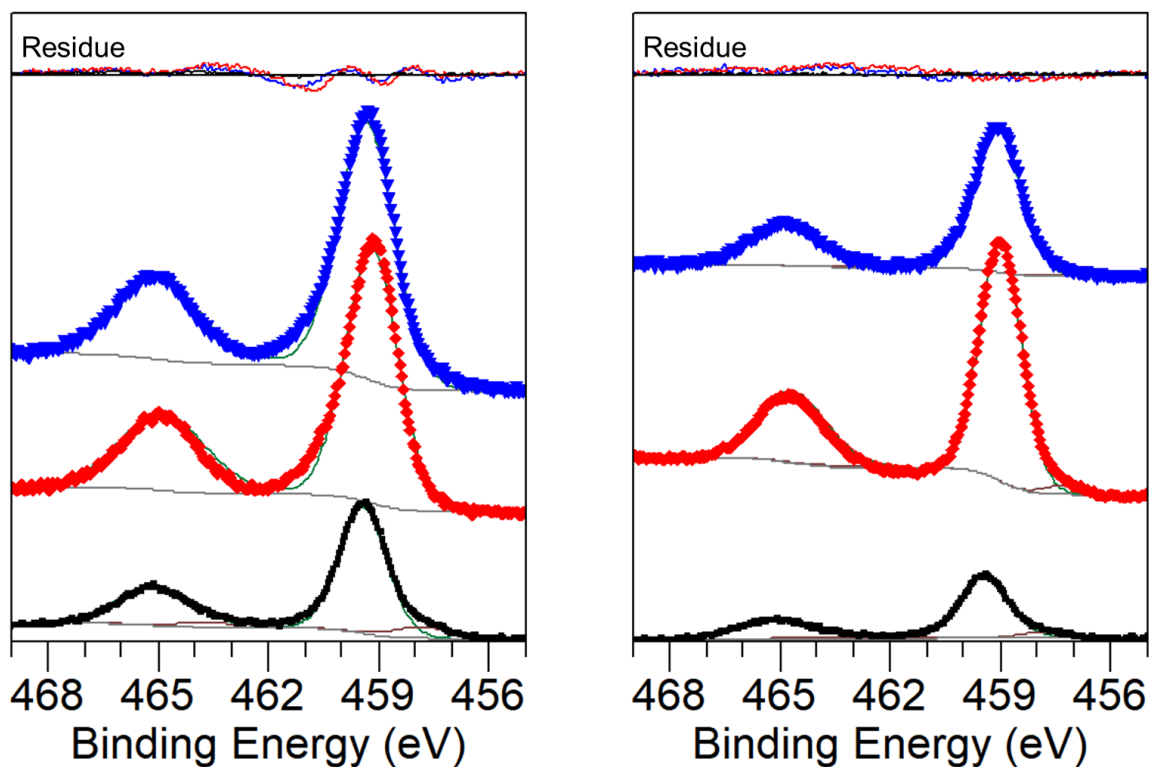
Figure S3. Alternative depiction of XPS spectra of Figure 6: Ti 2p X-ray photoelectron spectra of Ti_4O_7 (left) and Ti_6O_{11} (right) nanoparticles collected with a photon energy of 560 eV. Spectra are in the same order than on Figure 6. Experimental data are dots while components, backgrounds and envelopes are lines. The top graph shows the residues for the three spectra.
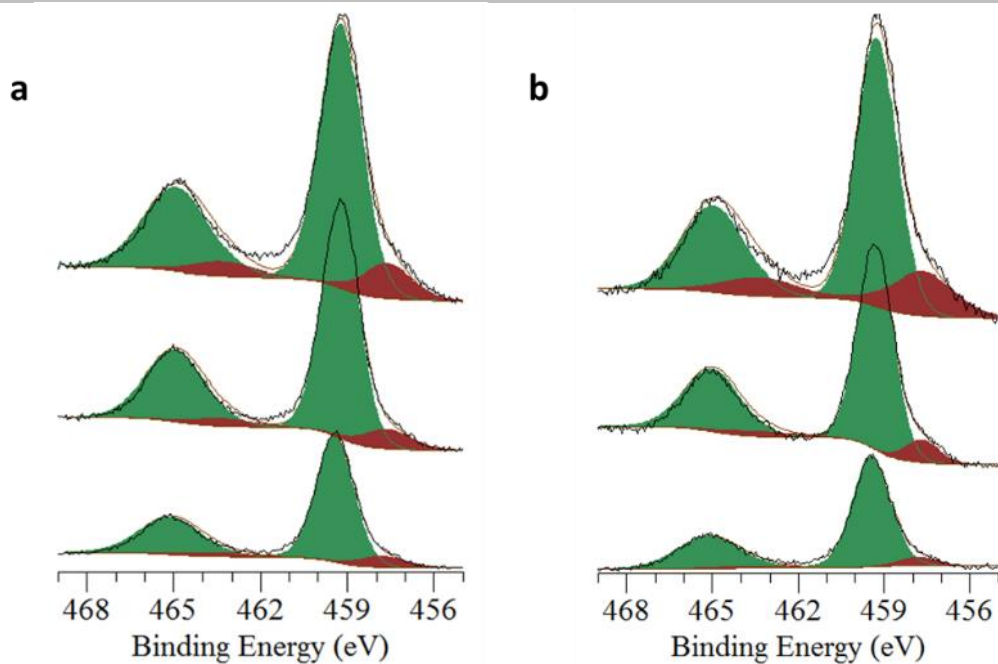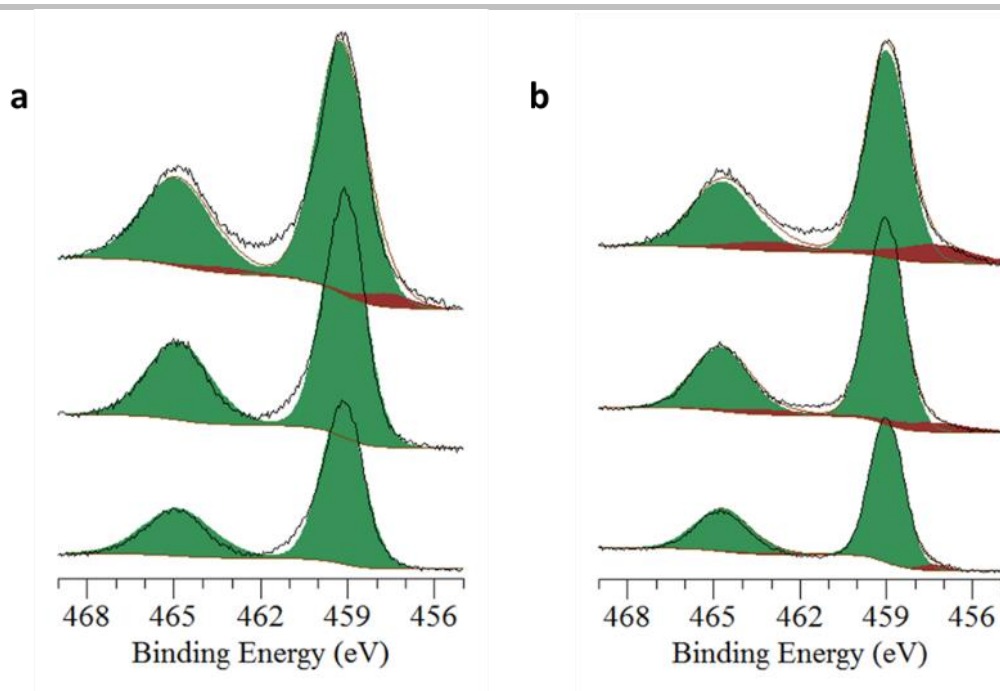
Figure S4. Ti 2p XPS region of (a) Ti_4O_7 and (b) Ti_6O_{11} nanoparticles at the initial state probed with different energies. From bottom to top: 560, 735 and 950 eV, corresponding to 0.6, 0.9 and 1.3 nm probed depths (IMFPs), respectively. Ti(IV) species are in green and Ti(III) species in brown.
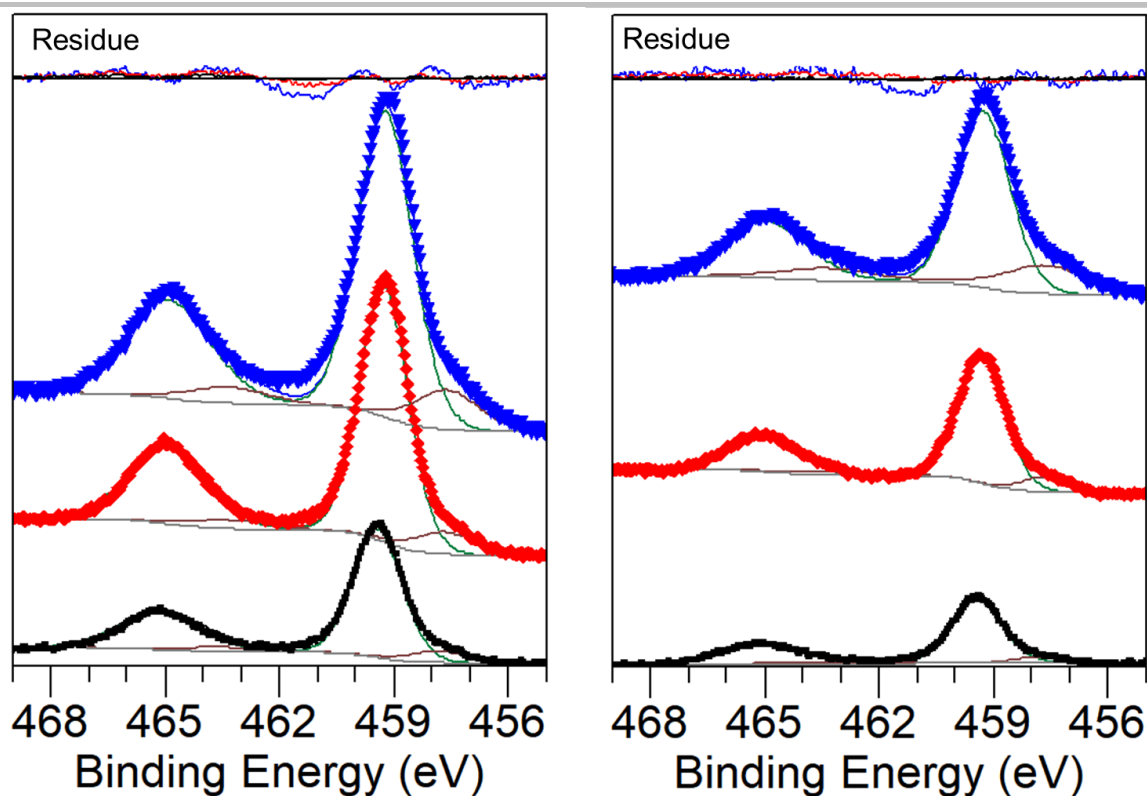
Figure S5. Alternative depiction of XPS spectra of Figure S4: Ti 2p XPS region of (left) Ti_4O_7 and (right) Ti_6O_{11} nanoparticles at the initial state probed with different energies. From bottom to top: 560, 735 and 950 eV, corresponding to 0.6, 0.9 and 1.3 nm probed depths (IMFPs), respectively. Experimental data are dots while components, backgrounds and envelopes are lines. The top graph shows the residues for the three spectra.
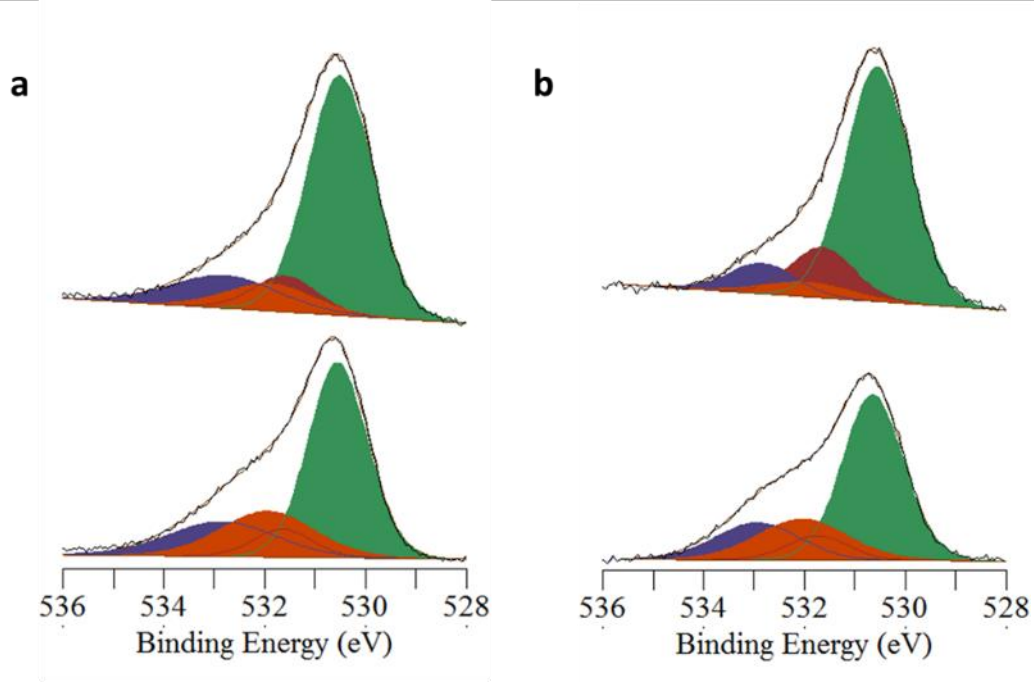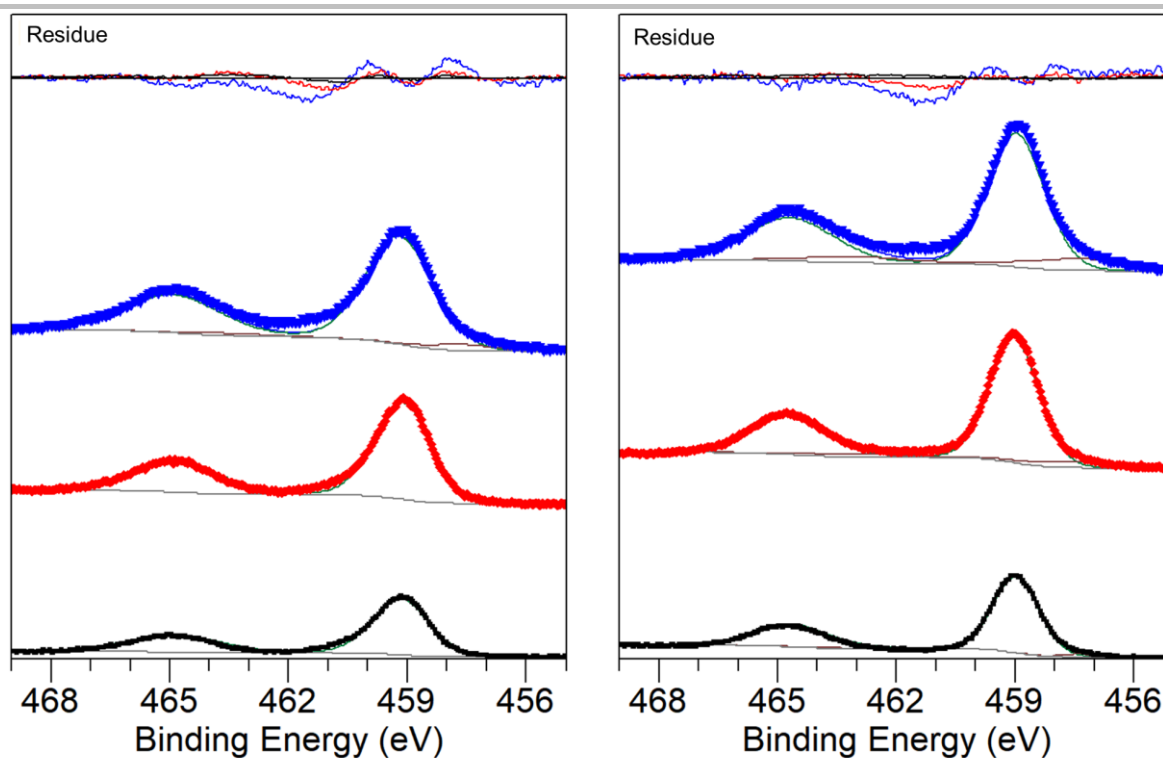
Figure S6. O 1s XPS region of (a) Ti_4O_7 and (b) Ti_6O_{11} nanoparticles at the initial state probed with different energies. From bottom to top: 735 and 950 eV, with similar probed depths (IMFPs) than for the Ti 2p signal. Green, dark red, light red and blue contributions at 530.5, 531.8, 532.0, 533.0 eV correspond to O-Ti(IV), O-Ti(III), HO-Ti and adsorbed H_2O, respectively.[Pouilleau, J., Devilliers, D., Groult, H. & Marcus, P. Surface study of a titanium-based ceramic electrode material by X-ray photoelectron spectroscopy. *J. Mater. Sci.* **32,** 5645–5651 (1997); Kuznetsov, M. V., Zhuravlev, J. F. & Gubanov, V. A. XPS analysis of adsorption of oxygen molecules on the surface of Ti and TiN_x films in vacuum. *J. Electron Spectros. Relat. Phenomena* **58,** 169–176 (1992).] The O-Ti(III) signal appears for large probed depth (~1.3 nm, top spectra), below the oxidized surface.

Figure S7. Ti 2p XPS region of (a) Ti_4O_7 and (b) Ti_6O_{11} nanoparticles after oxidation under O_2 (0.2 mbar) at 390 °C at the initial state probed with different energies. From bottom to top: 560, 735 and 950 eV, corresponding to 0.6, 0.9 and 1.3 nm probed depths (IMFPs), respectively.

Figure S8. Alternative depiction of XPS spectra of Figure S7: Ti 2p XPS region of (left) Ti_4O_7 and (right) Ti_6O_{11} nanoparticles after oxidation under O_2 (0.2 mbar) at 390 °C at the initial state probed with different energies. From bottom to top: 560, 735 and 950 eV, corresponding to 0.6, 0.9 and 1.3 nm probed depths (IMFPs), respectively. Experimental data are dots while components, backgrounds and envelopes are lines. The top graph shows the residues for the three spectra.